Title:

**Numerical study of spatiotemporal distortions in noncollinear optical parametric chirped-pulse amplifiers**

Authors:

Achut Giree, Mark Mero, Gunnar Arisholm, Marc J. J. Vrakking, and Federico J. Furch

**Final manuscript**

The original publication may be found at:

Journal: Optics Express Vol. 25, Issue 4, pp. 3104-3121 (2017)

DOI: https://doi.org/10.1364/OE.25.003104

# Numerical study of spatiotemporal distortions in noncollinear optical parametric chirped-pulse amplifiers

ACHUT GIREE,[1,2,*] MARK MERO,[1] GUNNAR ARISHOLM,[3] MARC J. J. VRAKKING,[1] AND FEDERICO J. FURCH[1]

[1]*Max Born Institute, Max-Born-Str. 2A, 12489 Berlin, Germany*
[2]*Amplitude Technologies, 2-4 rue du Bois Chaland CE 2926, 91029 Evry, France*
[3]*Norwegian Defence Research Establishment (FFI), PO Box 25, 2027 Kjeller, Norway*
**giree@mbi-berlin.de*

**Abstract:** During amplification in a noncollinear optical parametric amplifier the spatial and temporal coordinates of the amplified field are inherently coupled. These couplings or distortions can limit the peak intensity, among other things. In this work, a numerical study of the spatiotemporal distortions in BBO-based noncollinear optical parametric chirped-pulse amplifiers (NOPCPAs) is presented for a wide range of parameters and for different amplification conditions. It is shown that for Gaussian pump beams, gain saturation introduces strong distortions and high conversion efficiency always comes at the price of strong spatiotemporal couplings which drastically reduce the peak intensity even when pulse fronts of the pump and the signal are matched. However, high conversion efficiencies with minimum spatiotemporal distortions can still be achieved with flat-top pump beam profiles.



**OCIS Codes:** (190.4970) Parametric oscillators and amplifiers; (320.7110) Ultrafast nonlinear optics.

## References and Links

1. E. Riedle, M. Beutter, S. Lochbrunner, J. Piel, S. Schenkl, S. Spörlein, and W. Zinth, "Generation of 10 to 50 fs pulses tunable through all of the visible and the NIR," Appl. Phys. B **71**(3), 457-465 (2000).
2. D. Brida, C. Manzoni, G. Cirmi, M. Marangoni, S. Bonora, P. Villoresi, S. De. Silvestri, and G. Cerullo, "Few-optical-cycle pulses tunable from the visible to the mid-infrared by optical parametric amplifiers," J. Opt. **12**, 013001 (2010).
3. M. Baudisch, B. Wolter, M. Pullen, M. Hemmer, and J. Biegert, "High power multi-color OPCPA source with simultaneous femtosecond deep-UV to mid-IR outputs," Opt. Lett. **41**(15), 3583-3586 (2016).
4. A. Dubietis, R. Butkus, and A. P. Piskarskas, "Trends in chirped pulse optical parametric amplification," IEEE J. Sel. Top. Quantum Electron. **12**(2), 163-172 (2006).
5. J. Rothhardt, S. Demmler, S. Hädrich, J. Limpert, and A. Tünnermann, "Octave-spanning OPCPA system delivering CEP-stable few-cycle pulses and 22 W of average power at 1 MHz repetition rate," Opt. Express **20**(10), 10870-10878 (2012).
6. F. J. Furch, S. Birkner, F. Kelkensberg, A. Giree, A. Anderson, C. P. Schulz, and M. J. J. Vrakking, "Carrier-envelope phase stable few-cycle pulses at 400 kHz for electron-ion coincidence experiments," Opt. Express **21**(19), 22671-22682 (2013).
7. S. Prinz, M. Haefner, C. Y. Teisset, R. Bessing, K. Michel, Y. Lee, X. T. Geng, S. Kim, D. E. Kim, T. Metzger, and M. Schultze, "CEP-stable, sub-6 fs, 300-kHz OPCPA system with more than 15 W of average power," Opt. Express **23**(2), 1388-1394 (2015).
8. M. Puppin, Y. Deng, O. Prochnow, J. Ahrens, T. Binhammer, U. Morgner, M. Krenz, M. Wolf, and R. Ernstorfer, "500 kHz OPCPA delivering tunable sub-20 fs pulses with 15 W average power based on an all ytterbium laser," Opt. Express **23**(2), 1491–1497 (2015).
9. M. Mero, F. Noack, F. Bach, V. Petrov, and M. J. J. Vrakking, "High-average-power, 50-fs parametric amplifier front-end at 1.55 μm," Opt. Express **23**(26), 33157-33163 (2015).
10. H. Höppner, A. Hage, T. Tanikawa, M. Schulz, R. Riedle, U. Teubner, and M. J. Prandolini, "An optical parametric chirped-pulse amplifier for seeding high repetition rate free-electron lasers," New J. Phys. **17**, 053020 (2015).
11. J. Ahrens, O. Prochnow, T. Binhammer, T. Lang, B. Schulz, M. Frede, and U. Morgner, "Multipass OPCPA system at 100 kHz pumped by a CPA-free solid-state amplifier," Opt. Express **24**(8), 8074-8080 (2016).
12. M. Krebs, S. Hädrich, S. Demmler, J. Rothhardt, A. Zaïr, L. Chipperfield, J. Limpert, and A. Tünnermann, "Towards isolated attosecond pulses at megahertz repetition rates," Nat. Photonics **7**(7), 555-559 (2013).

13. F. J. Furch, A. Giree, F. Morales, A. Anderson, Y. Wang, C. P. Schulz, and M. J. J. Vrakking, "Close to transform-limited, few-cycle 12 μJ pulses at 400 kHz for applications in ultrafast spectroscopy," Opt. Express **24**(17), 19293-19310 (2016).
14. S. Akturk, X. Gu, P. Bowlan, and R. Trebino, "Spatio-temporal couplings in ultrashort laser pulses," J. Opt. **12**, 093001 (2010).
15. I. P. Christov, "Propagation of femtosecond light pulses," Opt. Commun. **53**(6), 364-366 (1985).
16. S. Akturk, X. Gu, P. Gabolde, and R. Trebino, "The general theory of first-order spatio-temporal distortions of Gaussian pulses and beams," Opt. Express **13**(21), 8642–8661 (2005).
17. J. Bromage, C. Dorrer, and J. D. Zuegel, "Angular-dispersion-induced spatiotemporal aberrations in noncollinear optical parametric amplifiers," Opt. Lett. **35**(13), 2251–2253 (2010).
18. D. N. Schimpf, J. Rothhardt, J. Limpert, A. Tünnermann, and D. C. Hanna, "Theoretical analysis of the gain bandwidth for noncollinear parametric amplification of ultrafast pulses," J. Opt. Soc. Am. B **24**(11), 2837-2846 (2007).
19. A. Zaukevičius, V. Jukna, R. Antipenkov, V. Martinėnaitė, A. Varanavičius, A. Piskarskas, and G. Valiulis, "Manifestation of spatial chirp in femtosecond noncollinear optical parametric chirped-pulse amplifier, " J. Opt. Soc. Am. B **28**(12), 2902-2908 (2011).
20. A. Shirakawa, I. Sakane, and T. Kobayashi, "Pulse-front-matched optical parametric amplification for sub-10-fs pulse generation tunable in the visible and near infrared," Opt. Lett. **23**(16), 1292-1294 (1998).
21. O. Isaienko and E. Borguet, "Pulse-front matching of ultrabroadband near-infrared noncollinear optical parametric amplified pulses," J. Opt. Soc. Am. B **26**(5), 965-972 (2009).
22. P. Di Trapani, A. Andreoni, G. P. Banfi, C. Solcia, R. Danielius, A. Piskarskas, P. Foggi, M. Monguzzi, and C. Sozzi, "Group-velocity self-matching of femtosecond pulses in noncollinear parametric generation," Phys. Rev. A **51**, 3164 (1995).
23. G. Arisholm, "General numerical methods for simulating second-order nonlinear interactions in birefringent media," J. Opt. Soc. Am. B **14**(10), 2543-2549 (1997).
24. G. Arisholm, "Quantum noise initiation and macroscopic fluctuations in optical parametric oscillators," J. Opt. Soc. Am. B **16**(1), 117-127 (1999).
25. P. Schlup, J. Biegert, C. P. Hauri, G. Arisholm, and U. Keller, "Design of a sub-13-fs, multi-gigawatt chirped pulse optical parametric amplification system," App. Phys. B **79**(3), 285-288 (2004).
26. G. Arisholm, J. Biegert, P. Schulp, C. P. Hauri, and U. Keller, "Ultra-broadband chirped-pulse optical parametric amplifier with angularly dispersed beams," Opt. Express **12**(3), 518-530 (2004).
27. O. Chalus, P. K. Bates, and J. Biegert, "Design and simulation of few-cycle optical parametric chirped pulse amplification at mid-IR wavelengths," Opt. Express **16**(26), 21297-21304 (2008).
28. M. W. Haakestad, H. Fonnum, and E. Lippert, "Mid-infrared source with 0.2 J pulse energy based on nonlinear conversion of Q-switched pulses in $ZnGeP_2$," Opt. Express **22**(7), 8556-8564 (2014).
29. Z. Bor and B. Racz, "Group velocity dispersion in prisms and its application to pulse compression and travelling-wave excitation," Opt. Commun. **54**(3), 165-170 (1985).
30. X. Gu, S. Akturk, and R. Trebino, "Spatial chirp in ultrafast optics," Opt. Commun. **242**(4-6), 599-604 (2004).
31. S. Akturk, X. Gu, E. Zeek, and R. Trebino, "Pulse-front tilt caused by spatial and temporal chirp," Opt. Express **12**(19), 4399-4410 (2004).
32. J. Bromage, J. Rothhardt, S. Hädrich, C. Dorrer, C. Jocher, S. Demmler, J. Limpert, A. Tünnermann, and J. D. Zuegel, "Analysis and suppression of parasitic processes in noncollinear optical parametric amplifiers," Opt. Express **19**(18), 16797-16808 (2011).
33. T. Kobayashi and A. Baltuska, "Sub-5 fs pulse generation from a noncollinear optical parametric amplifier," Meas. Sci. Technol. **13**(11), 1671-1682 (2002).
34. V. Bagnoud, I. A. Begishev, M. J. Guardalben, J. Puth, and J. D. Zuegel, "5 Hz, >250 mJ optical parametric chirped-pulse amplifier at 1053 nm," Opt. Lett. **30**(14), 1843-1845 (2005).

## 1. Introduction

Over the past two decades, optical parametric amplification has become an attractive technique to generate ultrashort, tunable pulses over a broad wavelength range from the visible to the mid-infrared [1–3]. Optical parametric amplifiers offer several advantages over conventional laser amplifiers [4]. In particular, scaling of the average power and repetition rate is more easily achieved because of the highly reduced thermal load. In addition, noncollinear phase-matching offers a large gain bandwidth capable of supporting the amplification of few-cycle pulses. Therefore, in recent years noncollinear optical parametric amplification has become the technique of choice to amplify few-cycle pulses at high repetition rates (>>10 kHz) [5–11]. Furthermore, secondary sources based on noncollinear optical parametric amplifiers (NOPAs) have received increased interest, in particular, in strong field physics and attosecond science [6, 10–13].

Widely used components in ultrafast optics such as prisms, gratings and lenses all introduce spatiotemporal couplings, i.e. couplings between the spatial and temporal properties of the electromagnetic field [14]. Even the propagation of ultrashort pulses in vacuum may introduce spatiotemporal couplings, due to the wavelength-dependent diffraction of a beam with a finite size [15]. A rigorous theory has recently been developed [16] and several experimental techniques have been implemented to measure first-order spatiotemporal couplings [14]. In the case of NOPAs, spatiotemporal couplings naturally occur due to the noncollinear geometry. Since such couplings, often called spatiotemporal distortions or aberrations, degrade the achievable pulse duration and the peak intensity at focus, it is important to address this issue if NOPAs are to be used in research fields such as attosecond science, where a high peak intensity needs to be achieved with a limited available pulse energy when one operates at high repetition rates. Pioneering work by Bromage *et al.* [17] demonstrated experimentally that angular dispersion of the amplified signal beam can be eliminated if the NOPA is operated at a particular noncollinear angle, the so-called "magic angle" [18], where the group velocities of the signal and the idler beams are matched, leading to a broad amplification bandwidth. The experimental findings were supported by a simple numerical model. Numerical simulations supported by experimental results reported by Zaukevičius *et al.* [19] pointed out that at the magic angle pulse front tilt is still present, despite the vanishing angular dispersion, and can only be avoided by matching the pulse fronts of the pump and the signal. In that respect, experimental efforts to eliminate the pulse front tilt have been reported in the literature (see for example [20, 21]).

In this paper, a detailed numerical study of spatiotemporal distortions in noncollinear optical parametric chirped-pulse amplifiers (NOPCPAs) is presented, utilizing three-dimensional (3D) simulations. The studied NOPCPAs are based on amplification in β-barium borate (BBO) crystals under type-I phase matching. In all cases the amplifier is pumped at 515 nm and seeded with a broad-band pulse centered at 850 nm. The aim of our study is to characterize the spatiotemporal properties of the amplified field and to find guidelines for optimum amplifier design. It is investigated how spatiotemporal distortions in the amplified beam depend on experimental conditions such as noncollinear angle, pump beam size, phase-matching geometry, pulse front matching, and distortions in the seed beam and how they are related to gain saturation and back conversion. In section 2, different sources of spatiotemporal distortions in NOPCPAs are briefly reviewed. The numerical model used to simulate the amplifier and the numerical tools to characterize the distortions are introduced in section 3. In section 4, a single stage NOPCPA is analyzed for different noncollinear angles and beam sizes, and for different phase-matching configurations. Next, the influence of pulse-front matching and gain saturation is analyzed. In particular, the impacts of spectral shaping of the signal pulse and spatial shaping of the pump beam are analyzed in saturated amplifiers. In addition, it is discussed how spatiotemporal distortions from a first amplification stage influence a second amplification stage. Finally, a series of recommendations for the optimal design of a BBO-based NOPCPA are given based on the simulation results.

## 2. Spatiotemporal distortions in NOPCPA

The origins of spatiotemporal distortions in NOPCPAs have been known since the introduction of the technique [22]. The pulse front of the signal is shaped by the spatiotemporal distribution of the gain, so unless the pulse front of the pump is tilted to match the signal, the signal pulse front will end up being tilted with respect to its propagation direction. The combination of tilted pulse front and temporal chirp also leads to spatial chirp. In addition, phase-matching can contribute to further pulse front tilt through its direct impact on angular dispersion [17]. Detuning the noncollinear angle from the magic angle leads to an angularly dispersed amplified signal beam and accordingly tilts the pulse fronts. The effect is dominant for relatively small beam sizes and large detuning angles.

In addition to these effects, birefringence of the crystal causes spatial walk-off of the extraordinary beam. For example, in BBO under type-I phase matching, the pump beam shifts away from the optical axis. Furthermore, during propagation the pump and the signal beams get separated from each other in the walk-off plane due to the noncollinear configuration. Such spatial walk-off effects, in combination with temporal walk-off due to pump versus signal group-velocity mismatch, introduce additional spatiotemporal couplings. The spatiotemporal couplings due to the combined birefringent and temporal walk-off are present even if the pulse fronts of the pump and the signal are matched (e.g. in collinear amplification).

An analytical study of spatiotemporal distortions in NOPCPAs is difficult, since the coupled-wave equations for three-wave mixing can be solved analytically only under very restrictive assumptions or approximations. Analytical expressions for the analysis of first-order spatiotemporal distortions have been presented in [19]. However, for a complete study of spatiotemporal distortions under more realistic amplification conditions, numerical methods are indispensable. In this work, the nonlinear coupled-wave equations are solved in three dimensions, which allows studying all possible spatiotemporal distortions in NOPCPAs over a diverse range of parameters.

## 3. Numerical model and analysis tools

The numerical code, Sisyfos (SImulation SYstem For Optical Science) [23, 24] was used to simulate NOPCPAs. Prior to this work, this code was already utilized in several works [25–28], verifying its potential to simulate second-order frequency mixing, including the effects of pump depletion, walk-off, dispersion, diffraction, parasitic effects, and thermal effects. The program solves the coupled-wave equations in three dimensions in Fourier space. In the case of parametric amplification, it calculates the complex electric field distribution of the amplified signal, pump and idler beams, as well as parasitic second harmonics of the signal and the idler (optional). After modelling the amplifier, the complex electric field of the output signal in three dimensions ($x$, $y$ and $t$) is used for post-processing, where $x$ and $y$ refer to the transverse spatial coordinates and $t$ is the time.

For simplicity, the study of spatiotemporal couplings is often limited to the first-order. The definitions for first-order couplings introduced in this section and analyzed in the following one are focused on couplings occurring between the walk-off plane spatial coordinate (taken as the $x$-coordinate) and time. These results can be easily extended to the orthogonal $y$-coordinate. As the electric field can be represented in four different domains: ($x$, $t$), ($x$, $\omega$), ($k_x$, $t$) and ($k_x$, $\omega$), where $\omega$ and $k_x$ are angular and spatial frequencies, respectively, there are eight possible couplings when both amplitude and phase are considered. They are connected via Fourier transformations [16], and only two of them are independent. From these eight first-order distortions, pulse front tilt, spatial chirp and angular dispersion are most commonly encountered.

The pulse front tilt, which is the angle between the pulse front and the phase front, may be characterized by the slope of the profile in the ($x$, $t$) domain:

$$\tan\gamma = c\left(\frac{dt_0}{dx}\right)_{x_0}, \tag{1}$$

where $\gamma$ is the pulse front tilt angle, $c$ is the speed of light, $x_0$ is the center of the beam profile, and $t_0$ is the center of gravity of the temporal profile at a particular position. The pulse front tilt can arise from angular dispersion according to [29]:

$$\tan\gamma_0 = c\left(\frac{dk_{x0}}{d\omega}\right)_{\omega_0} = -\lambda_0\left(\frac{d\varepsilon}{d\lambda}\right)_{\lambda_0}, \tag{2}$$

where $\gamma_0$ refers to the pulse front tilt angle due to the angular dispersion only. $k_{x0}$ corresponds to the center of gravity of the spatial frequency profile for a particular angular frequency $\omega$, $\omega_0$ is the center frequency and $\varepsilon$ is the propagation angle of the spectral component $\lambda$ with respect to the center wavelength $\lambda_0$.

Spatial chirp refers to the coupling between spatial and spectral coordinates and can be characterized in the ($x$, $\omega$) domain by the spatial dispersion $\left(dx_0/d\omega\right)_{\omega_0}$ or analogously the frequency gradient $\left(d\omega_0/dx\right)_{x_0}$ [30]. If spatial and temporal chirp appear simultaneously, the combined effect of both phenomena induces pulse front tilt even in the absence of angular dispersion. For example, in the case of a field with a Gaussian spectrum and a Gaussian spatial profile, the overall pulse front tilt is given by [31]:

$$\left(\frac{dt_0}{dx}\right)_{x_0} = \left(\frac{dk_{x0}}{d\omega}\right)_{\omega_0} + \left(\frac{d^2\varphi}{d\omega^2}\right)_{\omega_0}\left(\frac{d\omega_0}{dx}\right)_{x_0}, \tag{3}$$

where $\varphi$ refers to the spectral phase.

For the analysis of the simulations presented in this work, the spatiotemporal distortions were divided into two groups: first-order distortions and higher-order distortions. In order to calculate linear distortions, the simulated field in the ($x$, $y$, $t$) domain was transformed to the other domains by Fourier transformation. Then, the slopes of the two-dimensional intensity profiles in the ($x$, $t$), ($x$, $\omega$) and ($k_x$, $\omega$) were calculated in order to obtain the pulse front tilt, spatial chirp and angular dispersion respectively in the walk-off plane. In principle, this method can be utilized to characterize nonlinear distortions as well, but the quantitative analysis would be cumbersome, with a rapidly increasing number of distortion terms for each expansion order that is included. Therefore, the Strehl ratio (SR) was used as a measure of the extent of both linear and nonlinear spatiotemporal distortions. The Strehl ratio was computed as:

$$SR = \frac{I}{I_0}, \tag{4}$$

where $I$ and $I_0$ are the peak intensities of the output signal beam with and without distortions, respectively at the focal plane of an ideal lens. The procedure to calculate the intensities is as follows: First, the amplified pulses are compressed uniformly across the spatial profile. For this, the spectral phase, $\varphi(x_{\max}, y_{\max}, \omega)$ was taken as a reference, where $(x_{\max}, y_{\max})$ corresponds to the position of maximal intensity within the beam profile. This reference phase was then subtracted at all positions across the beam profile, resulting in a Fourier transform-limited pulse duration at $(x_{\max}, y_{\max})$, but not necessarily at other positions within the beam profile. The distortion-free electric field $E_{df}(x', y', \omega')$ which is by definition separable in $(x', y')$ and $\omega'$, was constructed from the distorted field $E(x, y, \omega)$ by multiplying the position-averaged spectral distribution times the frequency-averaged spatial distribution, while the spectral phase was set to zero at all positions according to:

$$E_{df}(x', y', \omega') = \beta \sum_{\omega} \left|E(x', y', \omega)\right| \sum_{x,y} \left|E(x, y, \omega')\right|, \tag{5}$$

where $\beta$ is a normalization constant that ensures that both fields have the same energy. Then, both the distorted and the distortion-free field were focused under ideal conditions by solving Kirchoff's integral under the Fraunhofer approximation leading to the peak intensities $I$ and $I_0$

respectively. The Strehl ratio calculated in this manner [cf. Eq. (4)] is a measure of the extent of spatiotemporal distortions irrespective of the order. The ratio will be unity for an ideal distortion-free field and decreases if spatiotemporal distortions are present i.e. the stronger the spatiotemporal distortions, the lower the Strehl ratio.

## 4. Simulation results and analysis

For all the simulations the nonlinear material considered was BBO under type-I phase matching. The pump pulses had a Gaussian temporal profile with a Fourier transform-limited duration of 1 ps (FWHM) and a central wavelength of 515 nm. The broadband seed pulses had a Fourier transform-limited pulse duration of 10 fs (FWHM), a Gaussian spectral profile, and a central wavelength of 850 nm. They were positively chirped to 600 fs (FWHM), unless specified otherwise. The choice of the initial pulse parameters and the nonlinear material was motivated by widely available Ytterbium-doped amplifiers that are suitable to pump NOPCPAs in the visible and near infrared. Both the pump and seed beam profiles were Gaussian and the beam sizes were matched in all cases. Considering the limited pump pulse energy at high repetition rate, the beam waists (half width at $1/e^2$ of the peak intensity) on the BBO crystal were always <=1 mm.

### *4.1 Single stage NOPCPA*

First, a single stage NOPCPA was considered. The phase matching geometry was chosen to be a walk-off compensating (WOC) geometry [see Fig. 1 (a)], in which the asymmetry in the beam profile of the amplified signal due to birefringent walk-off is minimized [32]. In negative uniaxial crystals ($n_e < n_o$), the Poynting vector of the extraordinary wave subtends an angle with the propagation wave vector, effectively displacing the energy distribution of the field away from the optical axis. The displacement is towards the signal wave in WOC configuration which partially compensates the walk-off effect between the pump and the signal wave due to the noncollinear geometry. Meanwhile in non-walk-off compensating (NWOC) configuration, the Poynting vector of the pump points away from the signal, increasing the spatial walk-off effects [see Fig. 1(b)]. In the WOC configuration, second harmonic generation from both the signal and the idler is phase-matched, introducing modulations in the spectra and ultimately reducing the signal and the idler pulse energies. These parasitic effects have been considered in the simulations. In the case of broadband phase-matching, the pump and the signal beams propagate at an angle of 24.45° and 26.95° respectively with respect to the optical axis of the crystal.

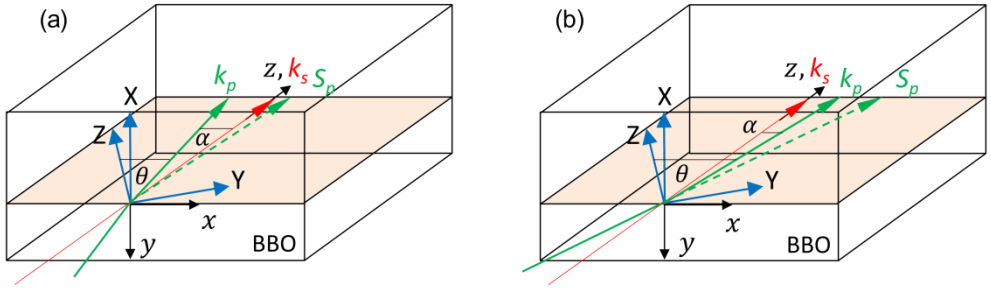


Fig. 1. Illustration of type-I phase matching geometries in a BBO crystal: (a) walk-off compensating (WOC) geometry and (b) non-walk-off compensating (NWOC) geometry. *X*, *Y*, *Z*: crystal axes of the BBO crystal; *x*, *y*, *z*: Cartesian co-ordinate system used in the calculations; $k_s$: signal wave vector that is incident perpendicularly to the crystal face, $k_p$: pump wave vector at an internal angle $\alpha$ with the signal wave vector and at the phase-matching angle $\theta$ with the optical axis (*Z*), and $S_p$: Poynting vector of the pump. All the vectors that relate to the laser propagation lie in the (*Y*, *Z*) or (*x*, *z*) plane. Not to scale.

For the first simulation, a 2 mm long crystal was pumped at a peak intensity of 40 GW/cm². For a beam waist of 500 µm, the pump pulse energy corresponds to 168 µJ. The seed pulse energy was chosen to be 8.4 nJ keeping the ratio of pump to seed pulse energy constant for all simulations. The effective nonlinear optical coefficient of BBO was taken to be 2 pm/V for both the OPA and the parasitic processes. The given set of parameters ensures that the gain is not saturated with 9% pump-to-signal energy conversion efficiency, which simplifies the analysis. The intensity profiles in different domains are shown in Fig. 2. It can be clearly seen that the distortions are almost linear and dominate along the walk-off plane [Figs. 2(d) and 2(e)] whereas distortions in the orthogonal plane are negligible [Figs. 2(b) and 2(c)]. Therefore, for the rest of the analysis of first-order distortions the attention is focused on effects arising in the walk-off plane. Note that the dips observed in the spatio-temporal and spatio-spectral profiles correspond to modulations in the spectrum due to parasitic effects. Since the slopes of the profiles directly reflect the first-order distortions, as explained in section 3, there is significant pulse front tilt [Fig. 2(d)], spatial chirp [Fig. 2(e)] and almost no angular dispersion [Fig. 2(f)] in the walk-off plane. These results are consistent with the results reported in [19].

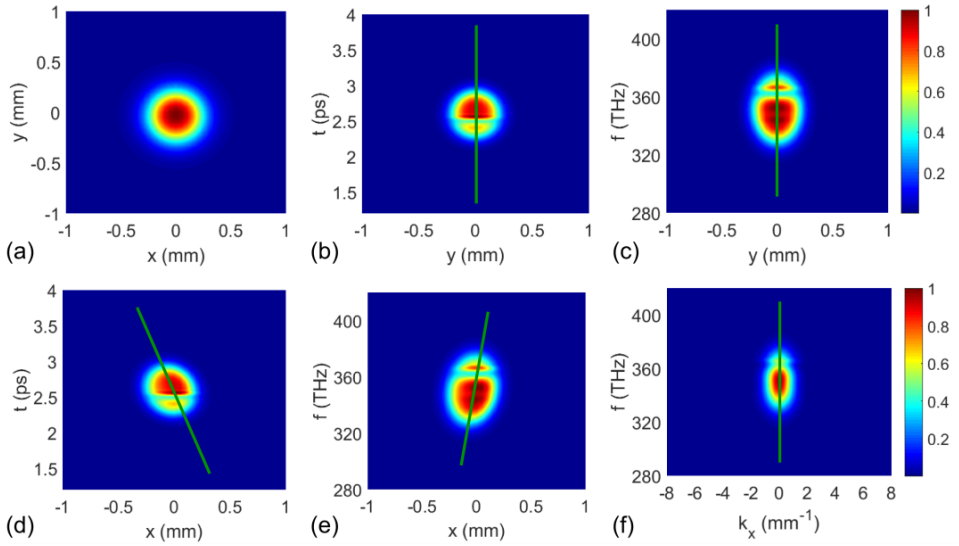


Fig. 2. Intensity profiles of the output signal from an unsaturated NOPCPA in different domains: (a) *y*-*x* (b) *t*-*y* (c) *f*-*y* (d) *t*-*x* (e) *f*-*x*, and (f) *f*-$k_x$ for an input beam waist of 500 µm (half width at 1/e$^2$ of peak intensity). The green lines are there to guide the eye. The output energy of the signal is 15.1 µJ (gain = 1800).

### *4.1.1 Influence of detuning the noncollinear angle*

The noncollinear angle was detuned from the magic angle and the above-mentioned calculation was repeated for four different beam waists of 125 µm, 250 µm, 500 µm and 1000 µm. These particular beam sizes were chosen in such a way that the smallest beam is comparable to the physical extension of the pump pulse and in order to cover several experimentally used pump beam sizes [6, 8]. For a peak intensity of 40 GW/cm², the pump pulse energies corresponding to the four different beam sizes are 10.5 µJ, 42 µJ, 168 µJ and 672 µJ respectively. In each case, first-order distortions were calculated from the spatiotemporal profiles as explained in section 3. The impact of detuning the noncollinear angle from the optimum value is shown in Fig. 3. Before compression, the overall pulse front tilt is significant in all cases [Fig. 3(a)]. After compression, the pulse front tilt decreases dramatically and is fully determined by angular dispersion [compare Figs. 3(b) and 3(d)]. Spatial chirp dominates for larger beam sizes [Fig. 3(c)] which has been discussed in [31].

The angular dispersion vanishes at the magic angle for all beam sizes and is approximately proportional to the detuning from the magic angle [Fig. 3(d)]. The variation is stronger for small beam sizes, which is mainly due to their large angular spectrum. These results are in good agreement with those reported in [17, 19].

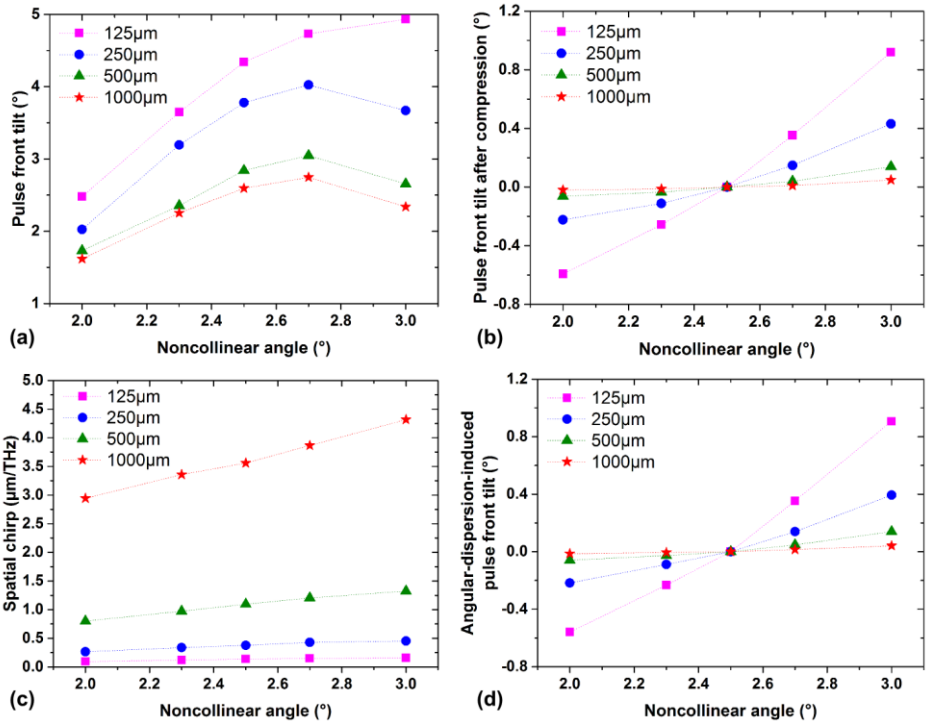


Fig. 3. Variation of spatiotemporal distortions with noncollinear angle in the walk-off compensating (WOC) geometry for an unsaturated NOPCPA, for various beam waist values (c. f. Legend): (a) pulse front tilt before compression and (b) pulse front tilt after compression; (c) spatial chirp and (d) angular dispersion-induced pulse front tilt. At the magic angle (2.5°) both the pulse front tilt and the angular dispersion are zero after compression.

In order to understand the influence of the phase matching geometry, this series of calculations was repeated for the NWOC configuration [see Fig. 1(b)]. The results are summarized in Fig. 4. Compared to the WOC configuration, a dramatic increase in the overall pulse front tilt is observed for small beam sizes [compare Figs. 3(a) and 4(a)]. This is mainly due to the larger spatial walk-off of the pump with respect to the signal, which increases the spatial chirp [compare Figs. 3(c) and 4(c)]. Nevertheless, after pulse compression the pulse front tilt is – as before – fully determined by angular dispersion [compare Figs. 4(b) and 4(d)]. However, away from the magic angle, the magnitude of the residual pulse front tilt due to angular dispersion is higher in the NWOC configuration than in the WOC configuration.

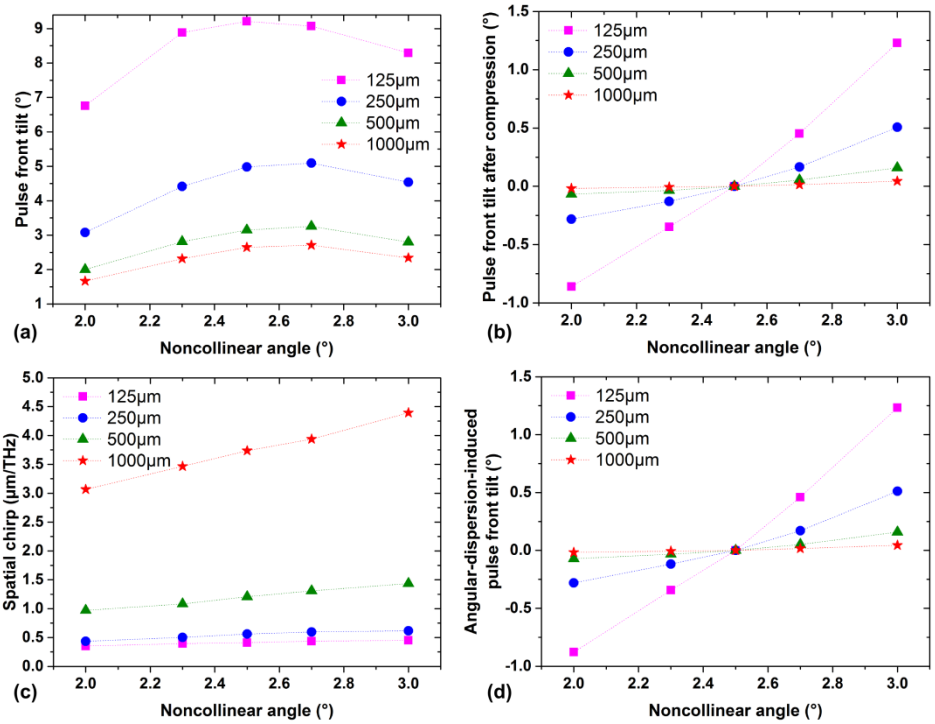


Fig. 4. Variation of spatiotemporal distortions with noncollinear angle in the non-walk-off compensating (NWOC) geometry for an unsaturated NOPCPA, for various beam waist values (cf. Legend): (a) pulse front tilt before compression and (b) pulse front tilt after compression; (c) spatial chirp and (d) angular dispersion-induced pulse front tilt. At the magic angle (2.5°) both the pulse front tilt and the angular dispersion are zero after compression. Away from the magic angle, the pulse front tilt and the angular dispersion increase more rapidly than in the WOC case [see Fig. 3].

### *4.1.2 Impact of pulse-front matching*

In addition to the group-velocity matching of the signal and the idler, pulse-front matching has been used in experiments to achieve tilt-free, spatially unchirped signal pulses from a noncollinear OPA [20, 21, 33]. Furthermore, numerical calculations show that matching the pulse fronts of the pump and the signal at the magic angle configuration minimizes the first-order distortions [19]. However, this has only been discussed for a particular set of parameters. In order to investigate the impact of pulse-front matching, simulations were performed by matching the pump and the signal pulse fronts in both phase matching configurations.

First-order distortions, for the case of matched pulse fronts are shown in Fig. 5 for the case of a NWOC configuration. It is found that matching the pulse fronts of the pump and the signal reduces the overall pulse front tilt [Fig. 5(a)]. This decrease in tilt is most significant for beam waists >250 µm, due to the strongly reduced spatial chirp, as can be seen in Fig. 5(c) compared to Fig. 4(c). In all cases, the overall pulse front tilt is only due to angular dispersion once the pulses are compressed [Fig. 5(b)], as seen in the previous calculations. However, there are no changes in the angular dispersion due to the pulse-front matching [compare Fig. 4(d) and 5(d)]. This is not surprising since the pump bandwidth is much smaller than the signal bandwidth, and the influence of angular dispersion introduced to the pump due to the tilted pulse fronts has negligible effect on the angular dispersion of the signal. Similar results were found in the case of WOC configuration (not shown). These results suggest that pulse-front matching is important only for beam waists >250 µm and in general, for beam sizes

considerably larger than the physical extension of the pump pulse. Of course, this only applies to the present analysis of linear distortions in unsaturated amplifiers.

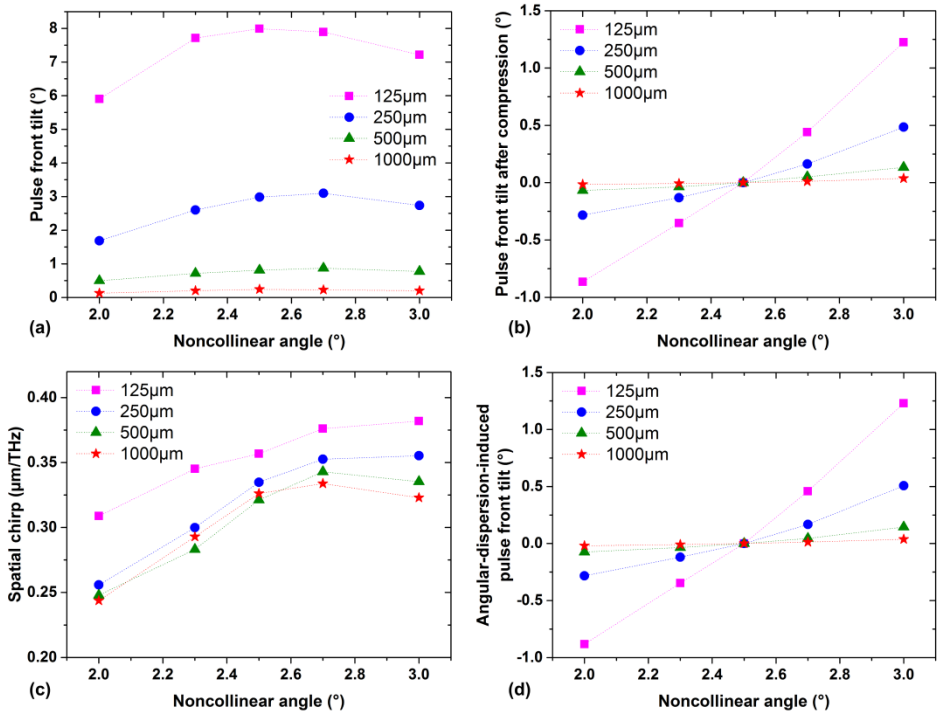


Fig. 5. Impact of pulse-front matching on linear distortions in an unsaturated NOPCPA in non-walk-off compensating (NWOC) geometry for various beam waist values (c. f. Legend): (a) pulse front tilt before compression and (b) pulse front tilt after compression; (c) spatial chirp and (d) angular dispersion-induced pulse front tilt, after pulse-front matching of the pump and the signal.

### *4.1.3 Influence of gain saturation*

The amplification conditions that have been considered so far did not include gain saturation. Amplifiers with gain saturation may introduce high order couplings. Still, this situation is of high practical interest since most amplifiers are operated in saturation. Gain saturation was simulated for both the WOC and NWOC configurations in two different approaches. In one case, the pump intensity was increased keeping all other parameters constant until the gain saturated and back conversion from the signal to the pump occurred, while in the other case, the length of the crystal was increased stepwise in order to saturate the gain at fixed pump intensity.

In the first approach, the crystal length was kept constant at 3 mm and the pump intensity was varied from 5 to 100 GW/cm² by increasing the pulse energy and keeping the beam waist constant at 500 µm. The rest of the parameters were identical to those used in the single stage NOPCPA modelled in section 4.1. The impact of different degrees of saturation on spatiotemporal distortions was characterized by calculating the Strehl ratio as described in section 3. Figure 6(a) depicts the evolution of the Strehl ratio and the conversion efficiency as a function of pump intensity in both the WOC and NWOC configurations. Gain saturation is clearly visible in the conversion efficiency in both configurations, whereas back conversion from the signal to the pump beam is visible in the NWOC configuration but not in the WOC configuration. Nevertheless, back conversion effects are observed in the WOC case in the temporal and spatial profiles of the pump and the signal. Additional simulations were also performed without considering parasitic effects. These calculations confirmed that strong

parasitic second harmonic generation of the idler beam considerably reduces the back conversion from the signal to the pump in the WOC configuration. The degradation of the Strehl ratio when the gain saturates, indicates that the impact of gain saturation on distortions is severe. This is all the more true in the regime where back conversion occurs. Even though the increase in pump intensity increases the conversion efficiency, the peak power that can be achieved is significantly reduced due to the distortions.

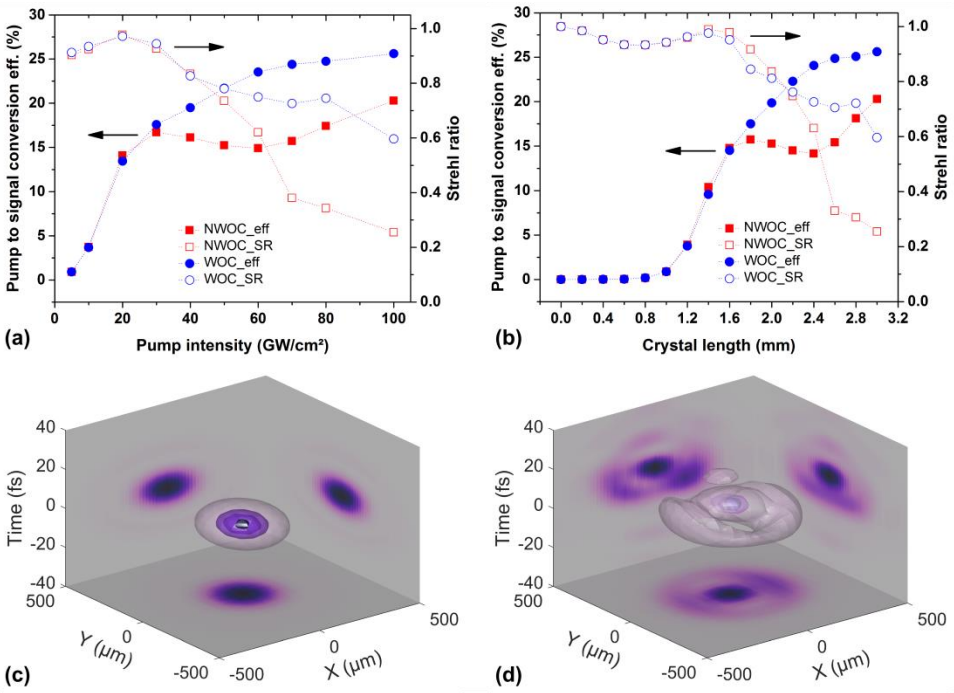


Fig. 6. The impact of gain saturation on spatiotemporal distortions in the walk-off compensating (WOC) and non-walk-off compensating (NWOC) configurations: (a) when the pump intensity is increased for a crystal length of 3 mm, and (b) when crystal length is increased keeping the peak pump intensity constant at 100 GW/cm$^2$. The conversion efficiency is shown on the left (solid blue circles for the WOC configuration and solid red squares for the NWOC configuration), revealing gain saturation for higher pump intensities (a) and longer crystal lengths (b). The accompanying Strehl ratios are shown on the right (open blue circles for the WOC configuration and open red squares for the NWOC configuration), revealing that the onset of gain saturation is accompanied by a significant reduction in the Strehl ratio. 'SR' and 'eff' refer to the Strehl ratio and the conversion efficiency respectively. Parts (c, d) illustrate the 3D spatiotemporal distribution after compression and focusing for crystal lengths of 1.8 mm (c) and 2.8 mm (d), both in NWOC configuration and for a pump intensity of 100 GW/cm².

In the second calculation, the pump intensity was kept constant at 100 GW/cm² (with a pulse energy of 418 μJ and beam waist of 500 μm) and the crystal length was increased from 0 to 3 mm in steps of 0.2 mm [Fig. 6(b)]. As was the case in Fig. 6(a), for increased crystal lengths the increase in conversion efficiency goes at the expense of a significant reduction of the Strehl ratio. In addition, Figs. 6(c) and 6(d) show the 3D spatiotemporal distribution after compression and focusing, for crystal lengths of 1.8 mm and 2.8 mm respectively, both in the NWOC case. The 3D objects in the figures were constructed by plotting surfaces of constant intensity. The panels at the planes x = 500 μm, y = 500 μm and t = -40 fs show 2D projections of the 3D distribution. The comparison between Figs. 6(c) and 6(d) illustrates how the spatiotemporal distribution, and hence the Strehl ratio, degrades when the crystal is longer than optimal.

Figure 6(b) indicates that at a pump intensity of 100 GW/cm², a Strehl ratio close to 1 can be maintained for crystal lengths shorter than 1.6 mm, which corresponds to conversion efficiency around 15% for both WOC and NWOC configurations. Up to a crystal length of 2 mm, there is a reasonable compromise between conversion efficiency and Strehl ratio. Beyond 2 mm, the Strehl ratio further degrades. The degradation is much more pronounced in the NWOC case while the conversion efficiency is higher in the WOC case. However, in the latter case, the amplified spectrum suffers from modulations due to the parasitic second harmonics. The evolution of the spatiotemporal couplings as the conversion efficiency increases can be illustrated also, by analyzing how the amplified spectrum varies within the beam profile along the walk-off coordinate. Figure 7 shows the spatio-spectral profiles for three different conversion efficiencies corresponding to crystal lengths of 1.4 mm, 1.8 mm and 2.8 mm [see Fig. 6(b)] and for both the NWOC and WOC configurations. In the NWOC case, the spectral modulations are mainly due to back conversion and more pronounced as the propagation length increases, while there is a strong dependence of the spectral shape on the spatial coordinate, as shown in Fig. 7(a). Furthermore, the amplified spectrum in the WOC case is modulated due to both back conversion and the parasitic second harmonics. As can be seen in Fig. 7(b), the variation of the spectrum within the beam profile is larger for higher conversion efficiency.

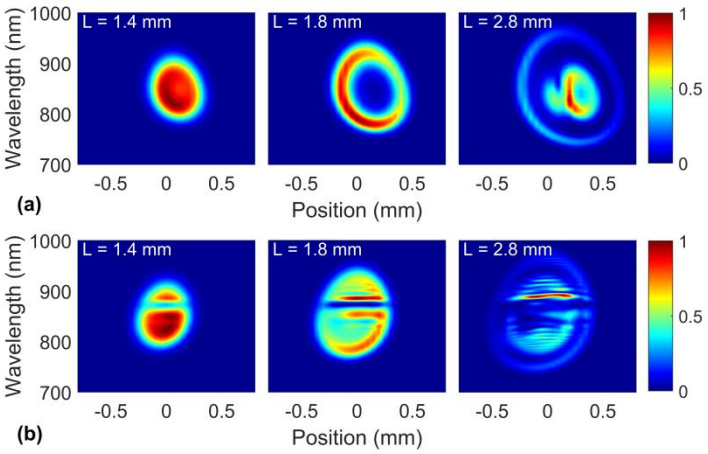


Fig. 7. Spatio-spectral profiles in the walk-off plane for three different conversion efficiencies corresponding to the crystal lengths (L) of 1.4 mm, 1.8 mm and 2.8 mm [see Fig. 6(b)] in the NWOC (a) and WOC (b) phase-matching configuration.

In addition, it is important to check whether the pulses are compressible. In order to compare the spectrum and the spectral phase in both configurations, a particular crystal length of 1.8 mm was chosen, for which the gain was already saturated but the Strehl ratio was better than 0.8 [Fig. 6(b)]. The complex electric field of the output signal at that crystal length was used to extract the spectrum and the spectral phase. First, a second order polynomial was fitted to the spectral phase at the center of the beam. The fitted phase $\varphi_f(\omega)$ was then subtracted from the total phase as:

$$\varphi(\omega) = \varphi(x_{\max}, y_{\max}, \omega) - \varphi_f(\omega), \tag{6}$$

$$\varphi_f(\omega) = a_0 + a_1\omega + a_2\omega^2, \tag{7}$$

where $\varphi(\omega)$ refers to the residual phase and $a_0$, $a_1$ and $a_2$ are the polynomial coefficients. Thus, only higher-order residual phase terms that need to be compensated to achieve the Fourier transform-limited pulse duration are left. The spectrum and the residual spectral phase at the center of the beam profile and the average spectrum are shown in Figs. 8(a) and 8(b) for

the NWOC and WOC configuration, respectively. The spectral phase at the center of the beam profile in the NWOC case seems well-behaved [Fig. 8(a)] and can readily be compensated, whereas the phase-jump resulting from the parasitic second harmonic in the WOC case [Fig. 8(b)] is challenging to compensate experimentally. This suggests that the NWOC configuration is more favorable for pulse compression. The pulses corresponding to the spectra at the center of the beam profile and the residual spectral phase, along with the Fourier transform-limited pulses as well as the near field beam profiles are shown in Figs. 8(c) and 8(d) for the NWOC and WOC configuration, respectively. The near field beam profile is less distorted in the WOC case as expected, however, a strong post pulse appears in the temporal profile. In the NWOC case, the pulse is close to being Fourier transform-limited.

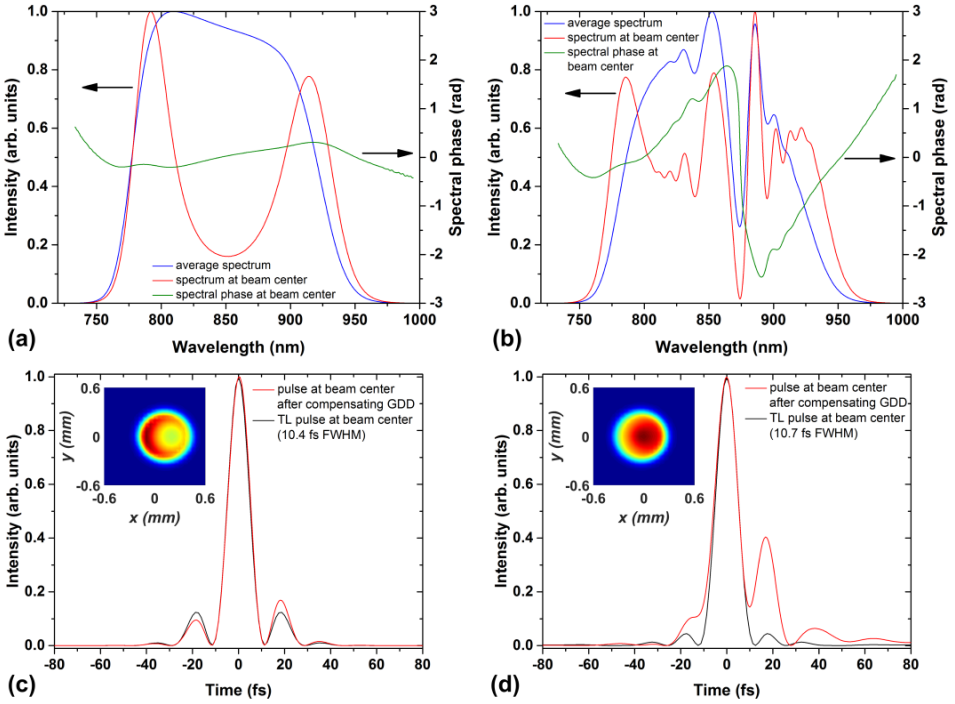


Fig. 8. Spectral and temporal characterization of the amplified signal beam, for a crystal length of 1.8 mm, and a pump intensity of 100 GW/cm² [a conversion efficiency over 15%, see Fig. 6(b)]: (a) Spectrum and spectral phase in the case of the NWOC and (b) the WOC configuration, (c, d) Temporal profiles corresponding to the spectrum at the center of the beam profile and the residual spectral phase (along with the Fourier transform-limited pulse) as well as the near field beam profile in the inset for (c) the NWOC and (d) the WOC configuration. The spectral phases in (a) and (b) correspond to higher-order dispersion terms, where the group delay dispersion has been removed.

From a practical point of view, these results point out that a conversion efficiency of 15-18% will ensure saturation, while keeping the Strehl ratio at acceptable values. Moreover, the NWOC configuration is the geometry of choice for better pulse compression, unless the walk-off effects degrade the beam quality.

### *4.1.4 Influence of beam/pulse shapes*

So far only Gaussian beams and Gaussian spectral (and temporal) shapes have been considered for the seed and the pump pulses. From a practical point of view it is interesting to study how saturation effects change with different beam shapes or spectral profiles. For example, the output of laser systems used to pump parametric amplifiers have, in some cases,

flat-top beam profiles (see for example [34]). In addition, the spectrum of broadband pulses is not Gaussian and it is often strongly modulated.

In order to study the impact of a modulated seed spectrum, a Gaussian spectral profile with a dip in the center was chosen which still supports Fourier transform-limited pulses of 10 fs (FWHM). The pulses were then chirped to 600 fs (FWHM). The beam shape of the seed was chosen to be Gaussian and the pulse energy was 8.4 nJ. The pump parameters were kept the same as in the previous section: Gaussian temporal shape with a duration of 1 ps (FWHM), pulse energy of 418 µJ and Gaussian beam profile focused to an intensity of 100 GW/cm² (beam waist of 500 µm). Figure 9 compares the conversion efficiency and Strehl ratio as a function of crystal length for three different seed spectra: 90% modulation depth, 50% modulation depth and no modulation (Gaussian shape), for the WOC and NWOC configuration. As can be clearly seen, there is very little influence of the spectral shape on the conversion efficiency and the Strehl ratio. On the one hand, these results imply that the conclusions from the previous section apply in general to more realistic spectral shapes. On the other hand, the implementation of existing techniques for spectral shaping would not have a strong impact in minimizing spatiotemporal couplings originated in saturated amplifiers.

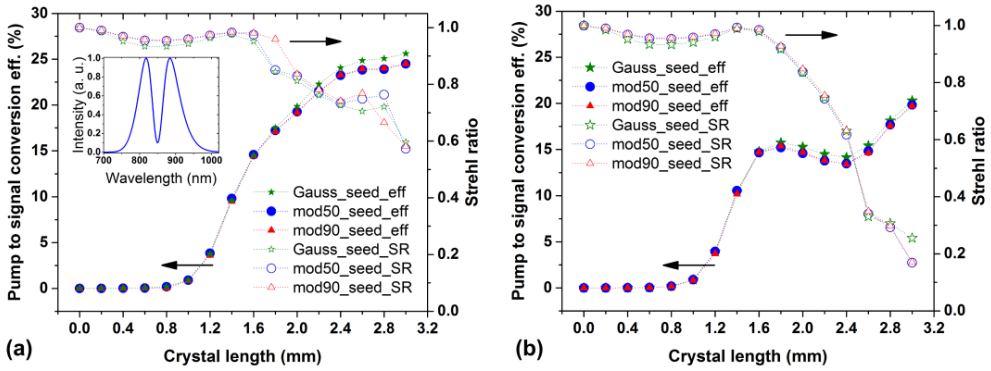


Fig. 9. Impact of gain saturation on conversion efficiency and Strehl ratio for three different seed spectra in the case of (a) WOC and (b) NWOC configuration. The inset shows a seed spectrum with 90% modulation depth. 'SR' and 'eff' refer to Strehl ratio and conversion efficiency, while 'Gauss_seed', 'mod50_seed' and 'mod90_seed' refer to the seed spectra without modulation, with 50% and 90% modulation depth respectively.

For the next set of simulations, the seed spectrum was Gaussian and all other seed parameters remained unchanged. Meanwhile the pump beam was changed to a supergaussian of order 10 with the aim of studying the impact of flat-top pump beam profiles. The pump pulse had a Gaussian temporal shape with pulse duration of 1 ps (FWHM) and the energy was increased to 668 µJ to keep the peak intensity constant at 100 GW/cm². Once again, the conversion efficiency and the Strehl ratio were calculated at each step along the crystal length and the results compared with those for a Gaussian pump beam as shown in Fig. 10. The homogenous gain across the seed beam due to the supergaussian pump beam profile allows a more efficient amplification for a given crystal length as compared to the Gaussian pump beam. Since the gain is relatively constant across the entire pump beam the energy transfer from pump to seed is spatially homogenous. That means that before reaching the back conversion regime, a significant amount of energy is transferred to the signal from the whole pump beam and not only from the center. As a result, a high conversion efficiency of around 25% can be achieved in both the WOC and NWOC configurations, while keeping a Strehl ratio higher than 0.9. The conversion efficiency can be increased even to more than 30% in the WOC case [Fig. 10(a)] without significant degradation of the Strehl ratio (higher than 0.85 for a crystal length of 2.2 mm). In the NWOC case however, the Strehl ratio degrades faster in the back conversion regime [Figure 10(b)].

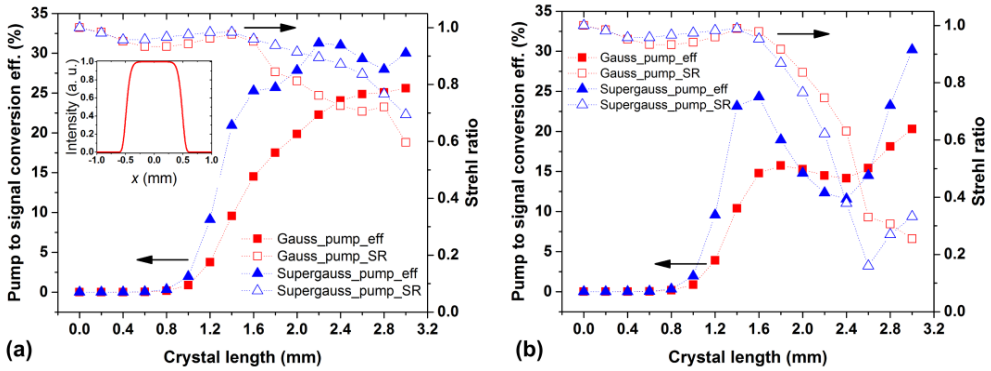


Fig. 10. Impact of gain saturation on conversion efficiency and Strehl ratio in the case of Gaussian and supergaussian pump beam of order 10 with a peak intensity of 100 GW/cm² in the (a) WOC configuration and (b) NWOC configuration. The inset shows a supergaussian pump beam profile. 'SR' and 'eff' refer to Strehl ratio and conversion efficiency, while 'Gauss_pump' and 'Supergauss_pump' refer to the Gaussian and supergaussian pump beam profile respectively.

### *4.2 Double stage NOPCPA*

NOPCPAs with output energy exceeding a few microjoules are mostly designed in a multi-stage scheme, therefore it is important to understand how the distortions carried over from one stage to the next affect the performance of the amplifier, in terms of spatiotemporal distortions. A double stage NOPCPA was modelled with the simulation parameters shown in Tab. 1. The pulse and beam shapes for the signal and pump were Gaussian. A pump intensity of 45 GW/cm² was used in both stages with the pump beam waists of 200 µm and 800 µm in the first and second stage respectively. An appropriate crystal length was chosen in order to investigate both unsaturated and saturated gain regimes. The primary focus is on the spatiotemporal distortions of the signal at the output of the second stage.

**Table 1. Parameters for two-stage NOPCPA simulations**

| | Parameter | Stage 1 | Stage 2 | |
|---|---|---|---|---|
| Signal | Center wavelength | 850 nm | Output signal from stage 1 after beam magnification | |
| | Pulse energy | 1 nJ | | |
| | Pulse duration (FWHM) | 600 fs chirped | | |
| | Bandwidth (FWHM) | 106 nm | | |
| | Beam waist | 200 µm | | |
| | Pulse and beam shapes | Gaussian | | |
| Pump | Center wavelength | 515 nm | | |
| | Pulse energy | 30 µJ | 480 µJ | |
| | Pulse duration (FWHM) | 1 ps (transform-limited) | | |
| | Beam waist | 200 µm | 800 µm | |
| | Pulse and beam shapes | Gaussian | | |
| BBO crystal | Length | 1.8 mm | 2.5 mm | |
| | $d_{eff}$ | 2 pm/V | | |
| Phase-matching (PM) parameters | PM configuration | WOC | WOC | NWOC |
| | PM angle | 26.95° | 26.95° | 21.95° |
| | Noncollinear angle | 2.5° | | |

At first, stage 1 was simulated as an unsaturated amplifier with a 1.8 mm long crystal so that the distortions at the output signal are almost linear. The output signal after beam magnification seeds the second stage which consists of a 2.5 mm long crystal. This crystal length ensures that the second amplifier is saturated, which allows the study of both unsaturated and saturated amplification by retrieving data from different positions along the crystal. Additionally, both WOC and NWOC configurations were considered in the second stage whereas the first stage was always in WOC configuration. Next, the length of the crystal in stage 1 was increased to 2.5 mm to saturate the gain and the output signal was used as the seed for the second stage.

### *4.2.1. Impact of distortions from the unsaturated first stage*

A crystal length of 1.8 mm in stage 1 ensured that the gain is not saturated as shown in Fig. 11(a). The pulse front tilt of the output signal after the first stage was ~232.7 fs/mm (4°) whereas the Strehl ratio was 0.97. After a magnification factor of 6, the output signal seeded the second stage under three different input cases and for both the WOC and NWOC configurations. For each case, the evolution of the Strehl ratio and the conversion efficiency are shown as a function of crystal length [Figs. 11(b) and 11(c)].

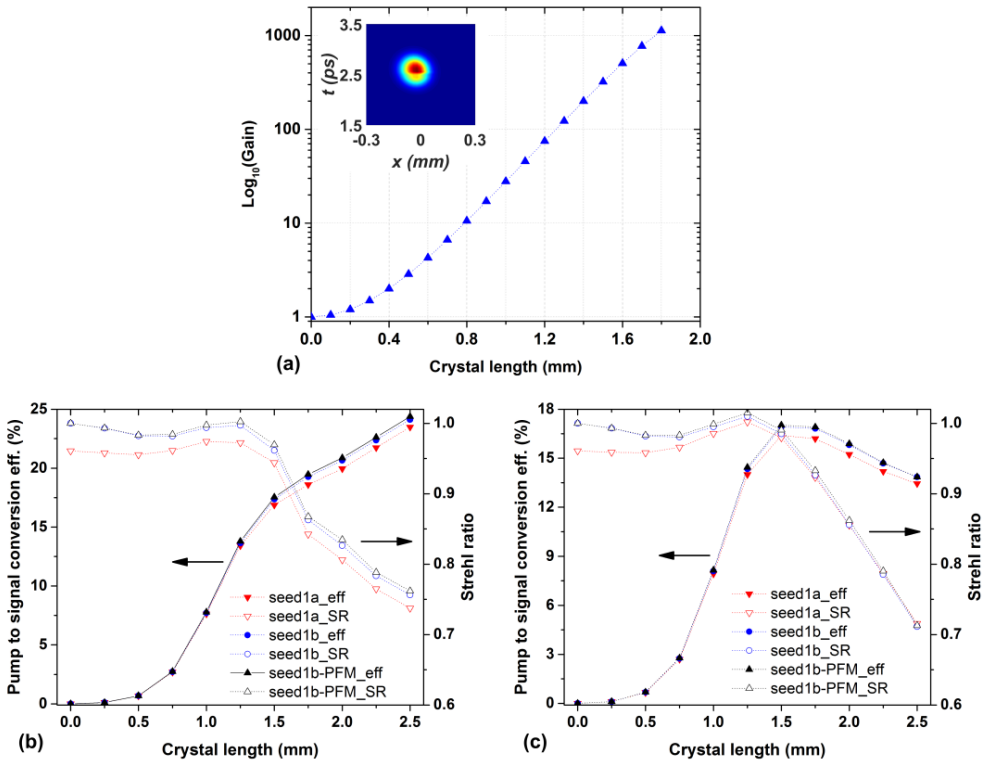


Fig. 11. Investigation of the impact of distortions from an unsaturated first amplification stage on the amplification and the output characteristics in a second stage: (a) gain of the first stage as a function of the crystal length, for a pump intensity of 45 GW/cm²; the inset shows the time-position profile of the output signal; (b) evolution of the Strehl ratio and the conversion efficiency in the second stage, for three input signal conditions (seed1a, seed1b and seed1b-PFM) in the WOC configuration and (c) in the NWOC configuration. The three input conditions for the second stage are given in the main text. 'SR', 'eff' and 'PFM' refer to the Strehl ratio, pump-to-signal energy conversion efficiency and pulse-front matching.

The three different input conditions were the following: (1) The output signal from the first stage seeded the second stage without any modifications (seed1a); (2) the distortions in

the output signal from the first stage were removed [cf. Eq. (5)] before seeding the second stage (seed1b); and (3) the distortions were removed from the seed and the pulse fronts of the seed and the pump were matched in the second stage (seed1b-PFM). For all crystal lengths of the second stage and for both configurations, the distortion-free seed performs slightly better than the distorted seed. The pulse-front matching of the pump and the distortion-free seed improves the conversion efficiency and the Strehl ratio even further, especially in the WOC case [Fig. 11(b)]. However, the effects of linear distortions in the seed are essentially negligible compared to the distortions introduced by gain saturation in the second stage. Since the degradation of Strehl ratio due to saturation dominates, pulse-front matching is not particularly useful in the case of saturated amplifiers.

### 4.2.2 Influence of distortions from the saturated first stage

The calculations in the previous section were repeated for the case where gain saturation also occurs in the first stage. The length of the crystal in the first stage was increased to 2.5 mm, so that the gain saturates without obvious back conversion as shown in Fig. 12(a). As mentioned in section 4.1.3, under these conditions there are higher-order distortions present in the output signal of the first stage and the Strehl ratio drops to 0.95.

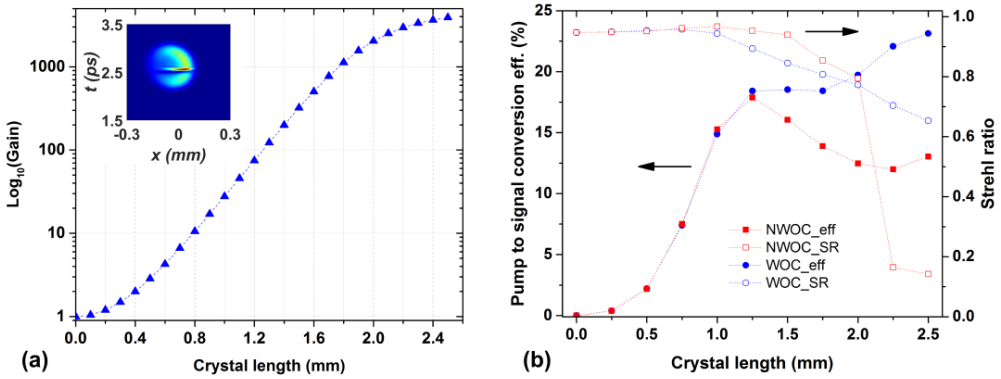


Fig. 12. (a) Evolution of gain with the crystal length in the saturated first stage; inset: time-position profile of the signal at the output of the 2.5 mm long crystal; (b) evolution of the Strehl ratio and the conversion efficiency of the output of the second stage in the WOC and NWOC configurations when the second stage is seeded with a distorted signal.

The distorted output signal was used to seed the second amplification stage. As expected, the gain now saturates at a shorter crystal length compared to the results of Fig. 11, given that the seed level is higher by a factor of 3.5. For longer crystal lengths, the Strehl ratio drops rapidly following the saturation behavior of conversion efficiency in both configurations [Fig. 12(b)]. In the unsaturated regime, the distortions in the output of the second stage are equivalent to the distortions in the seed as the Strehl ratio remains ~0.95 up to a conversion efficiency of ~15%. Once the gain saturates, the Strehl ratio with the saturated seed is slightly lower than the Strehl ratio for an unsaturated seed at the same conversion efficiency. The degradation of the Strehl ratio becomes worse when the back conversion to the pump is strong, clearly visible in the NWOC configuration. It should be noted that in the second stage the spatial and temporal profiles of the signal beyond a 2 mm crystal length are strongly modulated due to back conversion. Furthermore, the output spectrum in the WOC configuration is heavily modulated due to parasitic second harmonics.

It is clear that gain saturation dominates and degrades the Strehl ratio significantly. Additional simulations have shown that pulse-front matching doesn't improve the Strehl ratio despite minimizing the first-order distortions.

## 5. Summary and conclusions

A detailed numerical study of spatiotemporal distortions in BBO-based noncollinear optical parametric chirped-pulse amplifiers has been presented. Single stage and double stage amplifiers have been modelled under different amplification conditions and the spatiotemporal distortions in the amplified signal pulses have been characterized. As long as the amplifier is not saturated, the distortions at the output that are confined to the walk-off plane, are almost linear, and can be characterized by well-known parameters such as the pulse-front tilt angle, and constant spatial chirp and angular dispersion values. When the gain saturates, the distortions are no longer linear.

In amplifiers without strong gain saturation, angular dispersion vanishes at the magic noncollinear angle and increases with angular detuning, with a more pronounced effect for narrow beams. Pulse front tilt is significant for all noncollinear angles and pump beam sizes, but when the pulses are compressed the contribution from spatial chirp vanishes and only the contribution due to angular dispersion remains. Moreover, spatial chirp is always present for temporally chirped pulses, unless the pulse fronts of the pump and the signal are matched. Spatial chirp is particularly important for the case of a relatively large beam size. When the pulse is ideally compressed, the degradation of the Strehl ratio due to the first-order spatiotemporal distortions is not significant. However, gain saturation and particularly back conversion introduce strong higher-order distortions and degrade the Strehl ratio of the amplified signal beam. When the amplifier is deep into the back conversion regime, a situation arises where the peak intensity will be far from the maximum possible. If the amplifier gain is saturated, matching the pulse fronts of the pump and the signal does not appear to be important, for the particular range of beam waists and pulse duration used in this work.

If there are two amplification stages, the distortions from the unsaturated first stage play a minor role if the second stage is saturated. We conclude that it is convenient to build the first amplifier (or the first few amplifiers) in the WOC configuration and to operate them without strong saturation, so that the intensity of the amplified signal beam is not strong enough to drive efficient second harmonic generation, which degrades the spectral phase. On the other hand, a power (or last) amplifier should be built in the NWOC configuration if the best possible pulse compression is desired, whereas the WOC configuration should be chosen if the beam quality is more important. In both scenarios, the pump to signal energy conversion efficiency for Gaussian beams should be kept around 15% avoiding the back conversion regime if a degradation of the peak intensity higher than 10-20% due to spatiotemporal distortions is to be avoided. This scenario can be highly improved if a pump beam with flat-top profile is implemented. In that case conversion efficiencies as high as 25% can be achieved in both WOC and NWOC configuration, while keeping a Strehl ratio better than 0.9.

These results can be viewed as general guidelines for the development of BBO-based NOPCPAs with minimum spatiotemporal distortions. Furthermore, the described behavior can be qualitatively expected in any uniaxial crystal with dispersion properties similar to BBO.


## Funding

European Union- European Industrial Doctorate Program: Joint Max-Born Amplitude PhD Program (JMAP) (316687). This project has received funding from the Leibniz-Gemeinschaft grant no. SAW-2012-MBI-2 and from the European Union's Horizon 2020 research and innovation programme under grant agreement no. 654148 Laserlab-Europe.

## Acknowledgment

We would like to thank Jake Bromage from the Laboratory for Laser Energetics, Rochester, NY, USA, for useful discussions.